PHYSICAL REVIEW E **73**, 055304(R) (2006)

Fully nonlinear evolution of a cylindrical vortex sheet in incompressible Richtmyer–Meshkov instability

Chihiro Matsuoka[1] and Katsunobu Nishihara[2]
[1]*Department of Physics, Ehime University, Bunkyocho 2-5, Matsuyama 790-8577, Japan*
[2]*Institute of Laser Engineering, Osaka University, Yamada-oka 2-6, Suita, 565-0871, Japan*
(Received 16 March 2006; published 30 May 2006)

Fully nonlinear motion of a circular interface in incompressible Richtmyer–Meshkov instability is investigated by treating it as a nonuniform vortex sheet between two different fluids. There are many features in cylindrical geometry such as the existence of two independent spatial scales, radius and wavelength, and the ingoing and outgoing growth of bubbles and spikes. Geometrical complexities lead to the results that nonlinear dynamics of the vortex sheet is determined from the inward and outward motion rather than bubbles and spikes, and that the nonlinear growth strongly depends on mode number.

DOI: 10.1103/PhysRevE.73.055304 PACS number(s): 47.32.C−, 47.20.Ma, 02.70.Pt, 47.11.−j

The classical Richtmyer–Meshkov instability (RMI) [1] develops when a shock wave collides with a corrugated interface separating two different fluids. This instability is driven by the nonuniform vorticity left by the shock at the interface and in the fluids [2]. Namely, during the transition of the incident shock through the corrugated interface, the corrugation of the interface causes ripples on the fronts of transmitted and reflected shocks (or rarefaction wave), and the ripple of the fronts induces shear flow at the interface. A wide class of instabilities, not included in the shock-interface interaction, is still driven by the nonuniform vorticity on the interface, either initially deposited or supplied by external sources [3]. For example, in the experiments [4] shear flow was induced at an interface between incompressible fluids during the acceleration of a fluid container by a spring with a short but finite time duration. Also, in [5] nonuniform laser ablation caused shear flow at the ablation surface in laser implosions. These instabilities, caused by the nonuniform vorticity at the interface, are important in various areas such as astrophysical explosion, combustion, and inertial fusion implosions. We consider the nonlinear evolution of a nonuniform vortex sheet between different fluids in cylindrical geometry. The density ratio between the fluids essentially determines the nonlinear evolution of the instability due to the baroclinic effect. Moore *et al.* [6] showed that no disturbance grows for an expanding vortex sheet with uniform vorticity between the same fluids, a situation which corresponds to the Kelvin–Helmholtz instability.

Most previous works are focused on planar geometry [7–9] with only a few dealing with the effect of convergence in cylindrical geometry [10,11]. In addition to the convergence effects there are many features in cylindrical geometry, such as the existence of two independent spatial scales, i.e., the radius and wavelength, and also the ingoing and outgoing motion of bubbles and spikes. We will show that these geometrical complexities essentially determine fully nonlinear growth of the instability. In the nonlinear phase, the vortex interaction is nonlocal. Therefore, the interaction in cylindrical geometry may not be the same as that in an infinite periodic planar case. As will be shown, the nonlinear evolution of the vortex sheet is quite different for modes 1, 2, and higher. Here, we restrict ourselves to inviscid and incompressible fluids, and neither implosion nor explosion of the circular interface. Also, initial vorticity is nonuniformly distributed only at the interface. Despite these restrictions the study reveals many features of the nonlinear growth in cylindrical geometry.

The Bernoulli equation leads to the following equation for the circulation Γ on the interface [8,9]

$$\frac{d\Gamma}{dt} = 2A\frac{d\Phi}{dt} - A\boldsymbol{q}\cdot\boldsymbol{q} + \frac{A-2\alpha}{4}\boldsymbol{\kappa}\cdot\boldsymbol{\kappa} + \alpha A\boldsymbol{\kappa}\cdot\boldsymbol{q}, \qquad (1)$$

where $\boldsymbol{q}=(\boldsymbol{u_1}+\boldsymbol{u_2})/2$ is an average of the velocities of two fluids at the interface, which is related to the average velocity potential, $\Phi=(\phi_1+\phi_2)/2$ with $\boldsymbol{q}=\boldsymbol{\nabla}\Phi$, where $\phi_i(i=1,2)$ and $\boldsymbol{u_i}=\boldsymbol{\nabla}\phi_i$ are the velocity potential and the velocity of each fluid, respectively. The velocity potential satisfies $\Delta\phi_i=0$ in each region. The subscripts $i=1$ and $i=2$ correspond to the inner and outer fluids. We define the Atwood number as $A=(\rho_2-\rho_1)/(\rho_1+\rho_2)$ for two fluid densities ρ_i. Therefore, $A>0$ and $A<0$ correspond to a case of light inner fluid and heavy outer fluid, and vice versa. The circulation $\Gamma=\phi_1-\phi_2$ is related to the vorticity per unit length on the vortex sheet $\boldsymbol{\Omega}$ and the sheet strength (circulation density) κ as $\boldsymbol{\Omega}=-\boldsymbol{n}\times\boldsymbol{\nabla}\Gamma=-\boldsymbol{n}\boldsymbol{\kappa}=\kappa\hat{\boldsymbol{e}}_z$. The gradient is taken along the interface in the (r,θ) plane, and $\boldsymbol{n}$ and $\hat{\boldsymbol{e}}_z$ are unit vectors normal to the interface, and the z direction, respectively. The Lagrange differentiation d/dt in Eq. (1) is defined as $d/dt=\partial/\partial t+\bar{\boldsymbol{u}}\cdot\boldsymbol{\nabla}$, where $\bar{\boldsymbol{u}}=\boldsymbol{q}+\alpha\boldsymbol{\kappa}/2$. The artificial parameter α is a weighting factor, such that $\alpha=0$ for $A=0$, and $\alpha\neq 0$ for $A\neq 0$ [12]. The circulation is, therefore, conserved for the case of $A=0$. The factor α is related to the definition of the tangential velocity of the interface. Any values of the factor α satisfy the continuity condition of the normal velocity at the interface.

In the cylindrical coordinates (r,θ), the vortex-induced velocity, which equals the average velocity of the interface $\boldsymbol{q}$, is given by

$$q^r = \frac{-1}{2\pi}\int_0^{2\pi}\frac{\kappa'[r'\sin(\theta-\theta')]s'_\beta d\beta'}{r^2-2rr'\cos(\theta-\theta')+r'^2},$$

$$q^{\theta} = \frac{1}{2\pi}\int_0^{2\pi} \frac{\kappa'[r - r'\cos(\theta - \theta')]s'_{\beta}d\beta'}{r^2 - 2rr'\cos(\theta - \theta') + r'^2}, \tag{2}$$

from the Biot–Savart law. Here, β is a Lagrangian parameter that parametrizes the interface as $[r(\beta), \theta(\beta)]$, and s is the arc length of the interface, $s_{\beta} = \sqrt{r_{\beta}^2 + r^2\theta_{\beta}^2}$, where the subscript denotes the differentiation with respect to the variable. In Eqs. (2), the variables with the prime denote that they are functions with respect to β'. The interface velocity $\bar{\boldsymbol{u}} = (\bar{u^r}, \bar{u^{\theta}})$ is then given as

$$r_t \equiv \bar{u^r} = q^r + \frac{\alpha\kappa r_{\beta}}{2s_{\beta}},$$

$$r\theta_t \equiv \bar{u^{\theta}} = q^{\theta} + \frac{\alpha\kappa r\theta_{\beta}}{2s_{\beta}}, \tag{3}$$

following the planar case [12], where t denotes time. Equation (3) corresponds to the Birkhoff–Rott equation [15]. Differentiating Eq. (1) with respect to β and taking the relation of $\kappa = \partial\Gamma/\partial s = \Gamma_{\beta}/s_{\beta}$ [15] into account, we obtain the following Fredholm integral equation of the second kind:

$$\kappa_t = -\frac{2A}{s_{\beta}}(r_{\beta}q_t^r + r\theta_{\beta}q_t^{\theta}) - \frac{(1 - \alpha A)}{s_{\beta}^2}\kappa[(r_{\beta}q_{\beta}^r + r\theta_{\beta}q_{\beta}^{\theta}) + (rq^r\theta_{\beta}^2 - r_{\beta}\theta_{\beta}q^{\theta})] - \frac{A - \alpha}{4s_{\beta}}(\kappa^2)_{\beta}. \tag{4}$$

This equation coincides with the Euler equation when we choose the factor as $\alpha = -A$ [8].

By solving Eqs. (3) and (4) numerically, we can determine nonlinear motion of the nonuniform cylindrical vortex sheet between different fluids. It should be noted that Eqs. (3) and (4) are invariant for the normalization of r/r_0, tv_0/r_0, and v/v_0, where r_0 and v_0 are the initial radius of the interface and the initial growth rate, respectively. The initial growth rate v_0 corresponds to the linear growth rate of RMI for the wavelength of $\lambda = 2\pi r_0/n$ with the mode number n. Throughout the paper we use above normalization otherwise specified. This invariance may be related to the scaling law of RMI in cylindrical geometry found by Zhang *et al.* [11]. The authors have shown with the use of hydrodynamic simulations that the nonlinear growths of RMI scaled by the incident shock speeds, i.e., $v(\tilde{t})/v_s$ are the same in terms of the scaled time, $\tilde{t} = tv_s/r_0$, for various high Mach numbers of the incident shock. Since Zhang *et al.* fixed the mode number, the Atwood number, and the initial amplitude of the interface corrugation, the linear growth rates were determined only from the incident shock speed. The linear growth rates are roughly proportional to the incident shock speed for the high Mach numbers examined in their simulations, as pointed out by Wouchuk [16]. Therefore, the nonlinear growth of RMI can be also scaled by the incident shockspeed for their simulation conditions.

However, the nonlinear growth of RMI in cylindrical geometry depends strongly on the mode number, because of the existence of the two independent spatial scales. We, here, discuss the fully nonlinear evolution of the instability up to the normalized time $t = 2$ for various modes and different Atwood numbers. The linear growth rate of RMI is proportional to the corrugation amplitude, normalized by its wavelength. However, if the initial amplitude of the corrugation is much smaller than its wavelength, then the fully nonlinear evolution of the interface does not much depend on the initial amplitude [9]. As a result, we consider no corrugation of

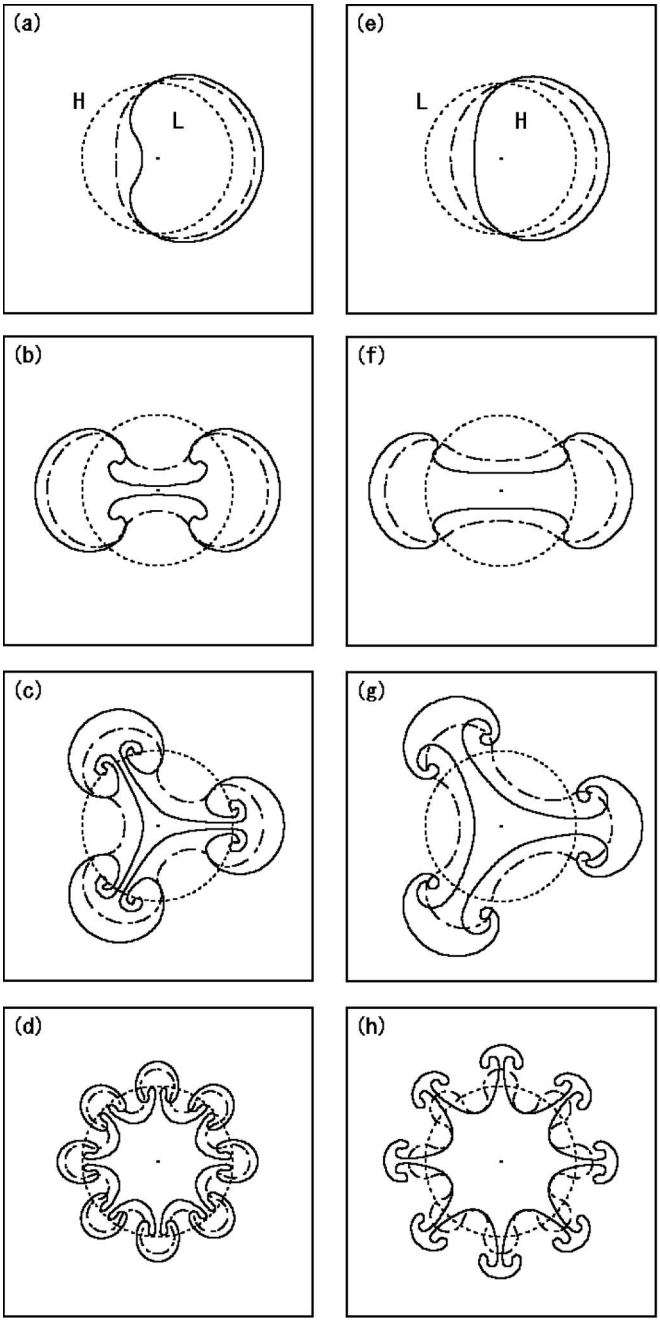

FIG. 1. Interfacial profiles for several modes: (a) $n = 1$, (b) $n = 2$, (c) $n = 3$, (d) $n = 8$ for $A = 0.2$, and (e)–(f) for the same modes for $A = -0.2$, where all dashed lines depict $t = 0$. The dot-dashed lines in (a) and (e) depict $t = 0.3$, while those lines in others depict $t = 0.8$. The solid lines in (a) and (e) depict $t = 0.52$, (b) and (f) show $t = 1.25$, and others show $t = 2.0$. All box sizes in the figures are $|x| \leq 2.0$ and $|y| \leq 2.0$. The letters "H" and "L" denote heavy and light fluids, respectively. The dots indicate the origin.

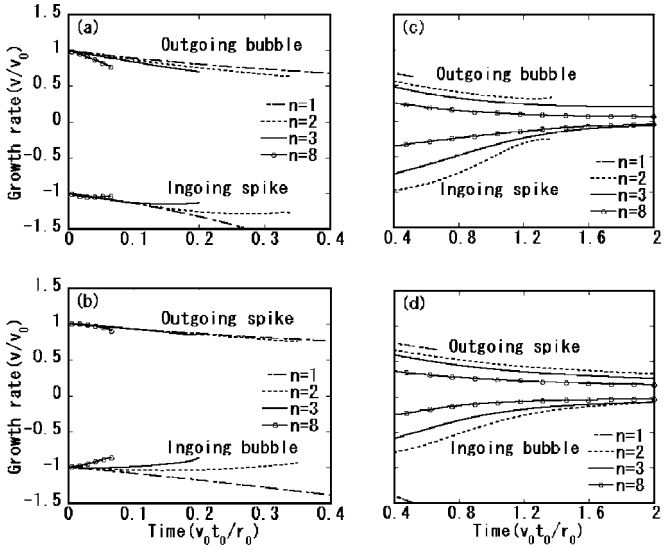

FIG. 2. Growth rates of bubbles and spikes for various modes: (a) and (c) $A=0.2$; (b) and (d) $A=-0.2$. The dot-dashed, dashed, solid, and solid with circles lines denote $n=1$, 2, 3, and 8, respectively.

the initial interface, but only the initial nonuniform velocity shear, corresponding to the initial growth rate, v_0, at the interface. The initial normalized conditions are then given as: $r(\beta,0)/r_0=1$, $\theta(\beta,0)=\beta$, $\kappa(\beta,0)/v_0=2\sin(n\beta)$ for the mode number n.

When we calculate the nonlinear dynamics of the vortex sheet up to the rollup, we regularize the denominators in Eqs. (2) as $r^2-2rr'\cos(\theta-\theta')+r'^2+\delta^2$ with a regularized parameter $\delta \ll 1$ introduced by Krasny [13]. This regularization with $\delta \neq 0$, called the vortex method, enables us to compute up to the fully nonlinear stage. However, the numerical result deviates from the analytical solution of the Euler equation. This deviation appears clearer at the initial stage, because the perturbation amplitude is initially very small. In order to avoid this deviation, we adopt the alternate point quadrature method, presented by Sidi and Israeli [14] for computations, in which we can set $\delta=0$. When we use this method, we choose the parameter $\alpha=-A$ for $A>0$ and $\alpha=A$ for $A<0$. In calculations when $\delta \neq 0$, we choose $\alpha=-A^2$ and $\alpha=A^2$ for $A>0$ and $A<0$, respectively. The number of grid points N in the computations is taken as $N=256n$ for the mode number n. For details of the methods in numerical calculations, refer to Ref. [9].

Figure 1 shows the temporal evolution of the interfacial profiles for various modes $n=1$, 2, 3, and 8, and the Atwood numbers $A=\pm 0.2$. Here we take the regularized parameter $\delta=0$ and $\delta=0.1$ in the calculations for mode $n=1$ and the others, respectively. For $A>0$ ($A<0$), the outgoing parts $\beta=(2m\pi)/n$, and the ingoing parts $\beta=(1+2m)\pi/n(m=0,\ldots,n-1)$, correspond to bubbles (spikes) and spikes (bubbles). The interface does not cross the origin for any of the modes in the incompressible cylindrical fluid, since the velocity potential is given as $\phi_1 \propto (r/r_0)^n \cos n\theta$ $(r<r_0)$, $\phi_2 \propto (r/r_0)^{-n} \cos n\theta$ $(r>r_0)$, so the modes diverge when the interface approaches the origin, which also causes breakdown of the calculation.

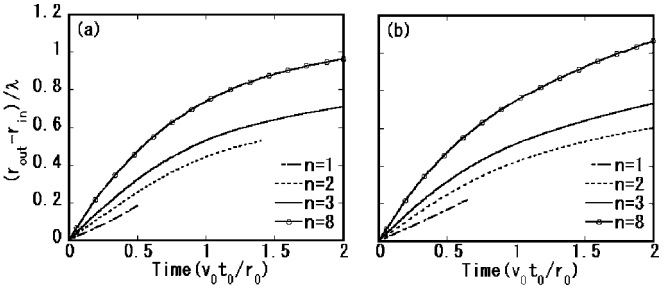

FIG. 3. Peak-to-valley amplitudes of various modes for (a) $A=0.2$ and (b) $A=-0.2$. The dot-dashed, dashed, solid, and solid with circles lines denote $n=1,2,3$, and 8, respectively.

The interface of mode $n=1$ does not roll up, which may relate to the fact that the strong concentration of the vorticity (κ in our calculations), that leads to the rollup, does not occur for mode $n=1$. The rollup of the interface begins approximately at the same normalized time of $t=1.0-1.2$ for all modes $n \geq 2$. In the planar case the interface rollup begins approximately at $t_p=2\pi v_0 t/\lambda=nv_0 t/r_0=2.4-2.5$. Therefore, the rollup in cylindrical geometry begins earlier than that in the planar one for lower modes $n \leq 3$, but later for higher modes $n \geq 4$.

In a planar case, the profiles of bubbles and spikes are quite different from each other. However, as shown in Fig. 1, the profile of the outgoing bubbles (ingoing spikes) for $A>0$ is not so different from those of the outgoing spikes (ingoing bubbles) for $A<0$. The interface profile in cylindrical geometry is, therefore, determined mainly from either outgoing or ingoing growth, regardless of the bubbles and spikes. The interface profiles at $t=2.0$ in Fig. 1 are also quite similar for $n \geq 3$. These results indicate that the fully nonlinear evolution of the growth in the cylindrical geometry is scaled by the initial growth rate v_0 and radius, instead of by the perturbation wavelength.

We show the nonlinear growth rates of bubbles and spikes for the same modes and $A=\pm 0.2$ in Fig. 2. We used $\delta=0$ for the calculations of $n=1$, and at the early stage shown in Figs. 2(a) and 2(b) for other modes. We used $\delta=0.1$ otherwise. The calculations with $\delta=0$ break down at early times for the higher modes. The breakdown times are almost the same as those in a planar case, if time is normalized by the wavelength. In a planar case, the nonlinear growth rate of the spike becomes larger than that of the bubble. However, in cylindrical geometry regardless of bubble and spike, the absolute values of the ingoing growth in Figs. 2(a) and 2(b) become once greater than the initial growth rate, and are larger than those of the outgoing growth that decreases monotonically. Namely, the growth rates are determined from the outgoing or ingoing motion rather than from bubble or spike, even for early stages.

At the fully nonlinear stages (c) and (d), the ingoing growth rates decrease very rapidly and tend to zero nearly at the normalized time of $t=2$ independently of modes, while the outgoing growth rates decrease more slowly and remain at relatively large values even at $t=2$. The ingoing growth rates decrease more rapidly for the higher modes. The outgoing growth rates remain at larger values at $t=2$, especially

for the lower modes. It should be also noted that the nonlinear growth of the outgoing spikes is larger than that of the outgoing bubbles in the fully nonlinear stage, even for cylindrical geometry. This difference of the growth rates between the outgoing bubble and spike can be also seen in Fig. 1 by comparing solid lines and dot-dashed lines between the cases of $A>0$ and $A<0$. The nonlinear growth of the ingoing spikes is also larger than that of the ingoing bubble as shown in Fig. 1, although its difference is smaller than that of the outgoing growth rates.

The peak-to-valley (PV) amplitudes of the perturbation normalized by the wavelength, $(r_{max}-r_{min})/\lambda$, are shown in Fig. 3, with respect to the normalized time for $A=\pm 0.2$. The difference of the initial growth of the amplitudes among the modes in Fig. 3 is attributed to time normalization. If we use time normalized by the wavelength instead of the radius, they are the same. In cylindrical geometry the higher modes have the larger PV amplitudes normalized by the wavelength even for the same linear growth rates. However, if the amplitudes are normalized by the initial radius r_0, the lower modes have the larger amplitudes, as also seen in their profiles in Fig. 1. The larger amplitudes for $A<0$ compared with those for $A>0$ are due to the larger growth rate of the outgoing spikes compared with that of the outgoing bubbles. The growth of the amplitudes decreases slowly, as expected from the nonlinear growth rates shown in Fig. 2. It should be noted that the PV amplitudes at time when the growth rates start to deviate from the initial value are different among the modes, approximately $(r_{max}-r_{min})/\lambda=0.3, 0.4$, and 0.5 for modes $n=2, 3$, and 8, respectively, as shown in Fig. 3. The corresponding value of the PV amplitude in planar geometry is approximately 0.4–0.5. The time when the deviation starts is earlier for higher modes in this normalized time.

In summary, we have investigated fully nonlinear dynamics of a nonuniform vortex sheet between different fluids in cylindrical geometry up to the normalized time of $tv_0/r_0=2$. The nonlinear growth is determined from the inward and outward motion rather than from bubble and spike, and this growth depends strongly on the mode number.

[1] R. D. Richtmyer, Commun. Pure Appl. Math. **13**, 297 (1960); E. E. Meshkov, Fluid Dyn. **4**, 101 (1969).
[2] J. G. Wouchuk and K. Nishihara, Phys. Plasmas **4**, 1028 (1997).
[3] A. L. Velikovich *et al.* Phys. Plasmas **7**, 1662 (2000), and many references therein.
[4] M. A. Jones and J. W. Jacobs, Phys. Fluids **9**, 3078 (1997).
[5] R. Ishizaki and K. Nishihara, Phys. Rev. Lett. **78**, 1920 (1997); V. N. Goncharov, *ibid.* **82**, 2091 (1999).
[6] D. W. Moore and R. Griffith-Jones, Mathematika **21**, 128 (1976).
[7] A. D. Kotelnikov, J. Ray, and N. J. Zabusky, Phys. Fluids **12**, 3245 (2000).
[8] C. Matsuoka, K. Nishihara, and Y. Fukuda, Phys. Rev. E **67**, 036301 (2003).
[9] C. Matsuoka and K. Nishihara, Phys. Rev. E **73**, 026304 (2006).
[10] J. R. Fincke *et al.*, Phys. Rev. Lett. **93**, 115003 (2004), and many references therein; N. E. Lanier *et al.* Phys. Plasmas **10**, 1816 (2003); S. H. R. Hosseini and K. Takayama, Phys. Fluids **17**, 084101 (2005).
[11] Q. Zhang and M. J. Graham, Phys. Rev. Lett. **79**, 2674 (1997); V. Zhakhovskii, K. Nishihara, and M. Abe, *Inertial Fusion Sciences and Applications 2001* (Elsevier, Amsterdam, 2002), pp. 106.
[12] G. R. Baker, D. I. Meiron, and S. A. Orszag, J. Fluid Mech. **123**, 477 (1982).
[13] R. Krasny, J. Fluid Mech. **184**, 123 (1987).
[14] A. Sidi and M. Israeli, J. Sci. Comput. **3**, 201 (1988).
[15] P. G. Saffman, *in Vortex Dynamics* (Cambridge University Press, Cambridge, 1992).
[16] J. G. Wouchuk, Phys. Plasmas **8**, 2890 (2001); Phys. Rev. E **63**, 056303 (2001).